A Quadruplet-Resonator-Based Ferrite-Free Choke for Suppressing Noise Currents on Cable Shielding

Ying-Cheng Tseng, Hui-Ling Ting, and Tzong-Lin Wu, *Fellow, IEEE*

***Abstract*—This paper presents a novel technique for suppressing cable noise currents, the quadruplet-resonator-based ferrite-free choke (QR-based FFC), to eliminate the gigahertz (GHz) electromagnetic interference caused by noise currents flowing on the cable shielding. This problem is difficult to handle with conventional ferrite materials since their permeabilities dramatically degrade when the operating frequency goes up to several GHz. In this paper, with the aid of QR surrounding on the cable shielding, the FFC forms bandstop responses against the noise currents. The corresponding equivalent lumped circuit model is proposed and investigated. Furthermore, the synthesis procedure is established using microwave filter theory. The QR-based FFC can achieve a high-level current suppression at the desired frequency band. This technology is experimentally verified: a given design example is demonstrated at the operating center frequency of 2.57 GHz. The frequency range of 3-dB current suppression is measured from 2.47 to 2.75 GHz (FBW = 10.8%), where the highest suppression level is up to 36 dB. The FFC-added cable also demonstrates a good result in the reduction of far-field radiation, where the reduction level of radiation peak gain is measured as 7 dB compared with that of a bare cable.**

***Index Terms*—Cable choke, ferrite free, quadruplet resonator (QR), radio-frequency interference (RFI).**

I. Introduction

THESE DAYS, with the urgent need for high-definition multimedia communication, high-speed input/output (I/O) interfaces, such as USB 3.1, Thunderbolt, HDMI, etc., have become the standard I/O interfaces of consumer electronics. Typically, shielded cables are required for those high-speed I/O interfaces to transmit high-speed data between master and client devices. [1]. Many studies show the cables plugging into electronic devices through connectors often induce severe electromagnetic-interference (EMI) or radio-frequency (RF)-interference (RFI) issues [2]–[4]. As these papers indicate, when the high-speed digital data pass across the connector interface into a cable, a voltage drop due to the inductive effect of the connector will be induced to generate the noise currents on the cable shielding. These noise currents that contribute to the unintended radiation are referred to as unbalanced currents [5] or common-mode currents [6] for different scenarios. Hereafter, we called them the noise currents to keep the generality. As the data rate of high-speed I/O interfaces goes higher and higher (several gigahertz (GHz) or even several tens of GHz), solving the EMI or RFI problems caused by the GHz noise currents becomes challenging and nontrivial.

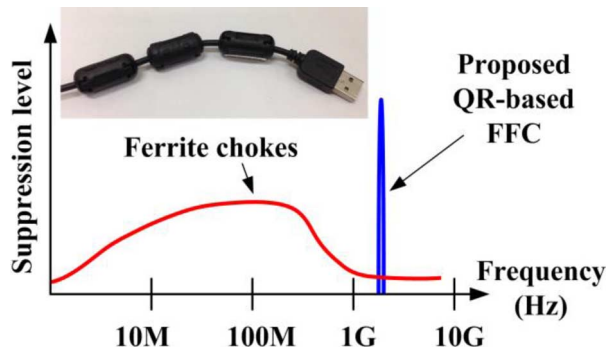

Fig. 1. Suppression comparison between ferrite chokes and the proposed QR-based FFCs.

Traditionally, utilizing the ferrite chokes to reduce the noise currents flowing on cable shielding is common. They are toroidal ferrite rings and are used to surround the cable that consists of the signal and ground shielding. The ferrite chokes have been widely applied in electronic industries for complying with EMI regulations [7], [8]. The high-permeability characteristic of ferrite chokes behaves as a high input impedance and, thus, the chokes can block the noise currents. However, since the permeabilities of ferrite materials rapidly degrade when the operating frequency goes higher, the function of the ferrite chokes, as shown in Fig. 1, is limited below GHz only.

On the other hand, to suppress the noise currents of interest up to GHz, cable balun chokes and sleeve structures were proposed [9]–[11]. They are generally applied for small antenna measurements in order to eliminate the noise currents radiating from cables. The core technology is to utilize quarter-wavelength resonant cavities or stubs to create the band-notch responses. To compose these structures, it requires bulky and heavy metallic tubes which are hard to employ in consumer or portable electronic devices.

In this paper, a novel ferrite-free choke (FFC) is proposed by utilizing quadruplet resonators (QRs) to uniformly surround the cable. When the resonance of QR occurs, the cable noise currents can be eliminated by the magnetic coupling between the cable and the QR. As Fig. 1 illustrates, compared with ferrite chokes, the noise currents on the cable shielding can be highly

Manuscript received March 19, 2015; revised July 21, 2015; accepted November 23, 2015. 20, 2015. Date of publication December 17, 2015; date of current version January 01, 2016. This work was supported by the National Science Council, Taiwan, under Grant 101-2221-E-002-127-MY3.

The authors are with the Department of Electrical Engineering and the Graduate Institute of Communication Engineering, National Taiwan University, Taipei 10617, Taiwan (e-mail: tlwu@ntu.edu.tw).

Color versions of one or more of the figures in this paper are available online at http://ieeexplore.ieee.org.

Digital Object Identifier 10.1109/TMTT.2015.2504447

suppressed at the specified GHz frequency band. Therefore, for practical applications, wideband noise suppression with specific narrowband noise elminiation can be simutaneously achieved using the combination of ferrite chokes and the proposed FFC.

This paper is organized as follows. Section II describes the noise radiation mechanism on a cable shielding. By taking coaxial cables as an example, an equivalent lumped circuit model including the coupling and the parallel LC tanks is proposed to explain the bandstop characteristics of the QR-based FFC in Section III. The susceptance slope parameters of the parallel LC tank (related to the stopband fractional bandwidth) can be extracted as a design chart by adjusting the coupling space between the QR and cable shielding. And, therefore, in Section IV, the systematic design procedure for designing a QR-based FFC is developed by employing a general filter synthesis method. The theoretical modeling and analysis will be illustrated in detail. In Section V, an FFC prototype based on the QR approach is realized. The capabilities of noise current elimination and radiation reduction are carefully measured to validate correctness of this new idea and corresponding theoretical models. Good agreement will be found in this section. Conclusions are drawn in Section VI.

II. Radiation Mechanism Caused by Cable Noise Currents

Fig. 2(a) shows the schematic of a wired communication system with a transmitter connected to a receiver through a coaxial cable. The coaxial cable consists of the inner signal line and outer ground shielding. The cable shielding (the outer conductor of the coaxial cable) is connected with the local ground, where there is a reference voltage plane for the transmitter and receiver, respectively. On the other hand, the global ground represents nearby large metallic objects, such as machine chases or infinity. As illustrated in Fig. 2(b), ideally, high-speed signals transmit inside the cable with the signal currents (I_{normal}) flowing on the inner signal conductor and return currents $(-I_{\text{normal}})$ flowing back on the shielding ground. When a current probe is encircled on the coaxial cable, the cable net current will be zero for the normal-mode operation due to Ampere's law. Practically, besides the normal-mode operation for high-speed signal transmission, the noise source (V_{noise}) is generated when the signal passes through discontinuous or unbalanced ground reference, such as from the printed-circuit board (PCB) ground of the transmitter circuit to the shielding ground of the coaxial cables and, thus, the cable noise currents (I_{noise}) will be induced as shown in Fig. 2(c). Such noise currents are also addressed as common-mode currents or unbalanced currents. In this case, the global ground can be considered as the return path of the noise currents (I_{noise}) via displacement currents [12]. Consequently, the noise currents flowing on the cable easily result in strong radiation and cause EMI or RFI issues since its return ground may be far away in practical circumstances.

III. Design Methodology for QR-Based FFC

As illustrated in Fig. 3(a), the proposed FFC utilizes the quadruplet half-wavelength resonators (QR) uniformly surrounding the cable shielding to achieve the purpose of noise

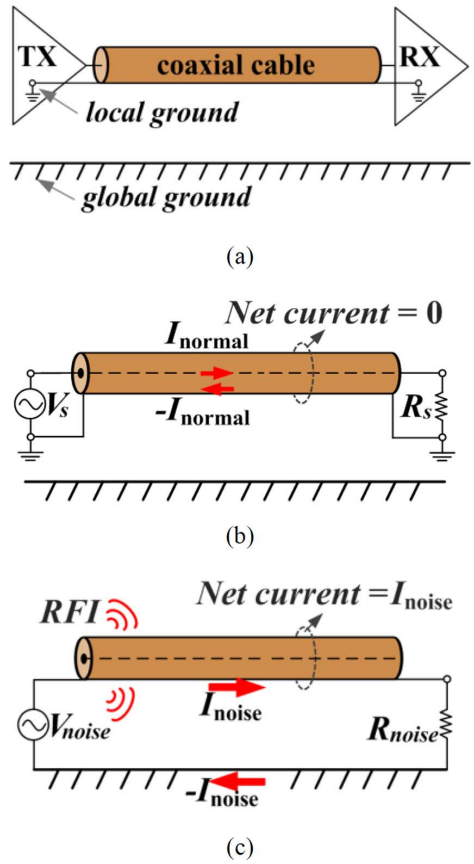

Fig. 2. (a) Schmatics of the wired communication system using a coaxial cable. (b) Normal-mode operation. (c) Noise-mode operation.

current suppression. Fig. 3(b) shows the cross-sectional view with an enlarged schematic for a single half-wavelength resonator. Each resonator, formed by a rectangular copper strip, is fabricated on a single-layer FR-4 substrate. The width of the strip and the spacing between two open ends of the strip are denoted as w and s_1, respectively. In addition, the spacing s_2 is the distance between the cable shielding and resonators.

In the case of a half-wavelength resonance, the middle point of the resonator strip typically has the peak magnitude for current distribution. The magnetic fields induced by the cable noise currents around the resonant frequencies will strongly couple to the quadruplet resonators, so the noise energy will be trapped into resonators (QR) and then reflected. To maximally achieve magnetic coupling, the normal direction of resonators is orthogonal to the axis of coaxial cable. On the other hand, by taking advantage of a strongly magnetic coupling mechanism, the resonator strips do not need to make direct contact with the cable shielding.

As described in Section II, the return path of the noise currents is on nearby large metallic objects or infinity; as a result, to build up systematic design procedures for those resonators, a large metallic plate is assumed below the cable with a distance h as the return path. Therefore, the propagation of noise currents can be modeled by transmission-line theory, where the signal trace of the transmission-line model is the cable shielding and the metallic plate is considered as its return path. The corresponding π-type model of this transmission line is shown in

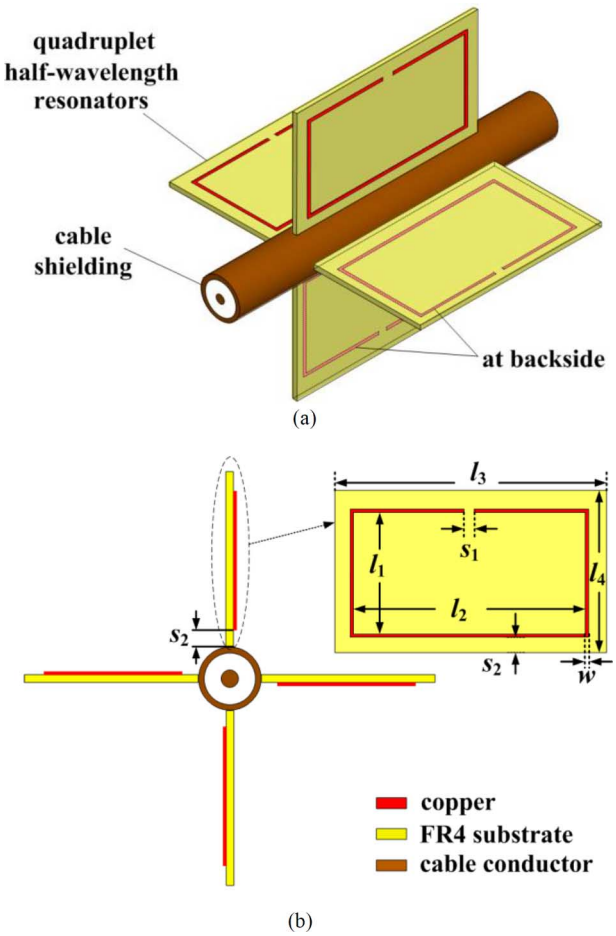

Fig. 3. Structure of the QR-based FFC: (a) oblique view and (b) cross-sectional view.

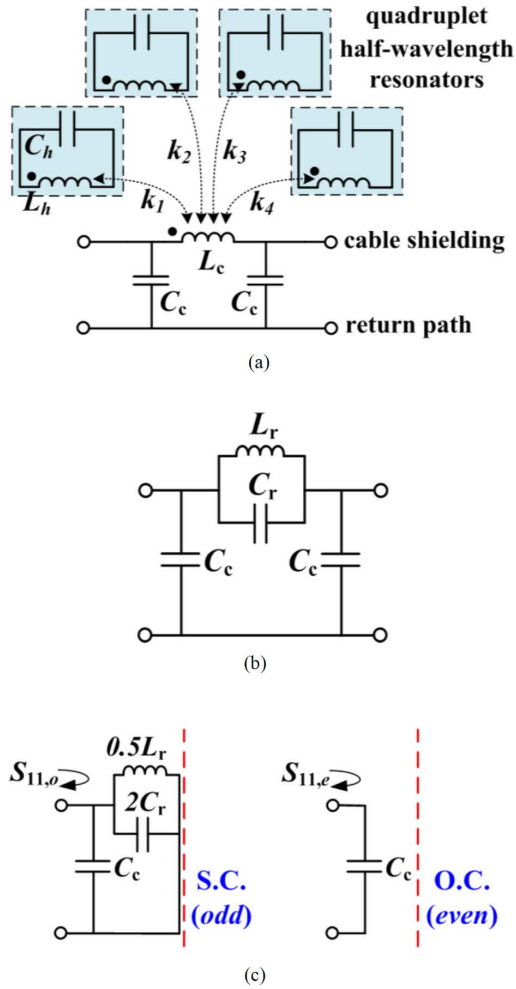

Fig. 4. Equivalent circuit models of the QR-based FFC: (a) full model, (b) simplified model, and (c) the corresponding even- and odd-mode models.

Fig. 4(a), where L_c is the inductance of cable shielding and the capacitor C_c is the capacitance formed between the cable shielding and the metallic plate. As shown in Fig. 4(a), each half-wavelength resonator can be represented by a lumped parallel LC circuit L_h and C_h. Dotted arrows indicate the magnetic coupling between the cable shielding and resonators, where the coupling between L_c and each individual L_h is marked with symbols k_j. (Subscript j stands for the jth resonator.)

For design simplicity, four resonators are designed to be identical and, therefore, their corresponding resonant frequencies are the same. By referring to the detailed derivations in the Appendix, the two-port network with the magnetic coupling circuit as shown in Fig. 4(a) can be equivalent to a simplified two-port network with a parallel LC tank of L_r and C_r, as plotted in Fig. 4(b). L_r and C_r can be related to the parameters in Fig. 4(a) by (A7) and (A8) as derived in the Appendix.

In accordance with the even- and odd-mode models plotted in Fig. 4(c), the frequency responses of reflection coefficient (S_{11}) and transmission coefficient (S_{21}) of the simplified model can be derived as

$$S_{11} = \frac{S_{11,e} + S_{11,o}}{2} \tag{1a}$$

$$S_{21} = \frac{S_{11,e} - S_{11,o}}{2} \tag{1b}$$

where $S_{11,e}$ and $S_{11,o}$ are the reflection coefficients of the even and odd modes, respectively, and can be expressed as

$$S_{11,e} = \frac{\frac{1}{Z_0} - j2\pi f C_c}{\frac{1}{Z_0} + j2\pi f C_c}, \tag{1c}$$

$$S_{11,o} = \frac{\frac{1}{Z_0} - j2\pi f (C_c + 2C_r) - \frac{2}{(j2\pi f L_r)}}{\frac{1}{Z_0} + j2\pi f (C_c + 2C_r) + \frac{2}{(j2\pi f L_r)}}. \tag{1d}$$

Through solving the frequencies of reflection zero $(S_{11} = 0)$ and transmission zero $(S_{21} = 0)$, denoted as f_{rz} and f_{tz}, respectively, the lumped values L_r and C_r of the simplified circuit model can be expressed in terms of $(Z_{\rm o}, C_c, f_{\rm rz}, f_{\rm tz})$ as

$$L_r = \frac{2C_c Z_0^2}{1 + (2\pi f_{rz} C_c Z_0)^2} \cdot \frac{f_{tz}^2 - f_{rz}^2}{f_{tz}^2}, \tag{2}$$

$$C_r = \frac{1}{(2\pi f_{tz})^2} L_r \tag{3}$$

where Z_0 is the characteristic impedance formed by the cable shielding and metallic plate. Equations (2) and (3) are used to extract the L_r and C_r values from the S-parameter responses by the full-wave simulation.

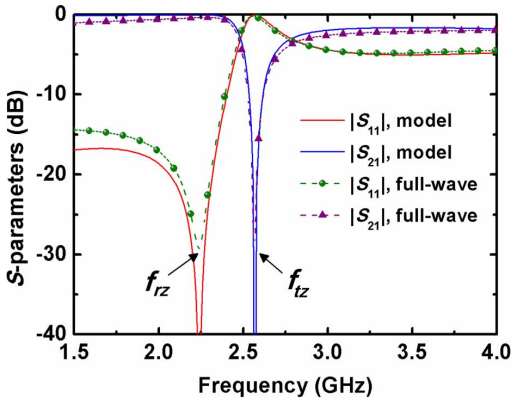

Fig. 5. S-parameters of the modeled and full-wave simulation.

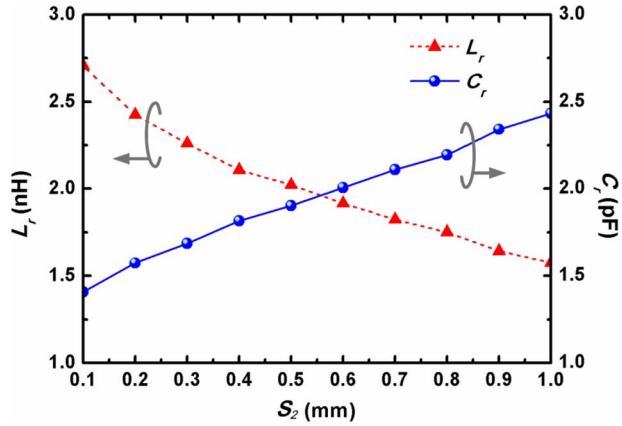

Fig. 6. Extracted values of L_r and C_r with different distances of s_2.

Fig. 5 shows the simulated S-parameters of an example of the QR-based FFC by a full-wave simulator *Ansys* HFSS 15.0. The substrate thickness for the resonators is 0.4 mm with $\epsilon_{\rm r} = 4.4$ and $\tan\delta = 0.02$. The detailed dimensions of the layout shown in Fig. 3 are $l_1 = 7.6$, $l_2 = 14.6$, $l_3 = 17$, $l_4 = 10$, $w = 0.2$, $s_1 = 0.2$, and $s_2 = 0.9$. The diameter of the inner conductor and cable shielding is 0.9 and 3.58, respectively. All units are in millimeters. The distance h between the cable shielding and the large metallic plate is set as 3 cm. It is found in Fig. 5 that the frequencies of $f_{\rm rz}$ and $f_{\rm tz}$ are 2.24 and 2.57 GHz, respectively, by full-wave simulation. In addition, Z_0 is solved as 180.4 Ω and C_c is extracted as 0.166 pF using the Q3D software [13]. By substituting those parameters into (2) and (3), the inductance of L_r and the capacitance of C_r are extracted as 2.26 nH and 1.686 pF. The S-parameters responses predicted by the simplified circuit model are also illustrated in Fig. 5. Compared with the full-wave results, the agreement between them is very good. It is found that the QR-based FFC has the bandstop characteristic for the noise currents around $f_{\rm tz} = 2.57$ GHz with a 3-dB fractional bandwidth (FBW) of 15%. This good consistency also implies that the simplified circuit model can well explain the noise suppression behavior of the QR-based FFC.

In fact, there is no specific limitation to the number of resonators. Basically, the resonators should fully surround the cables to have an effective noise suppression performance. However, more resonators will cause higher coupling between resonators and make the resonant mechanism too complicated to be understood. There is a tradeoff for choosing the resonator number. In our experience, the proposed quadruplet (four) resonators is the better setup with lower mutual coupling between resonators and with acceptable surrounding of the cable.

For the following section, the quadruplet resonators (QR) and the corresponding simplified circuit model will be utilized as a unit cell for the synthesis of the multiorder bandstop filter. The L_r and C_r values can be easily tuned by changing the spacing s_2 between the resonators and the cable shielding to control the coupling level. In other words, the susceptance slope parameter of the (L_r, C_r) parallel tank can be well adjusted by changing the distance s_2. Fig. 6 shows an example of the dependency of L_r and C_r variation on the distance s_2 for the aforementioned resonators with a half-wavelength resonance at $f_{\rm tz} = 2.57$ GHz. It is seen that L_r decreases from 2.75 to 1.5 nH as s_2 increases from 0.1 to 1.0 mm. Since L_r and C_r follow the relation of (2), the capacitance C_r is increased accordingly when the spacing is increased. This information is essential for the synthesis of following multiorder QR-based FFC.

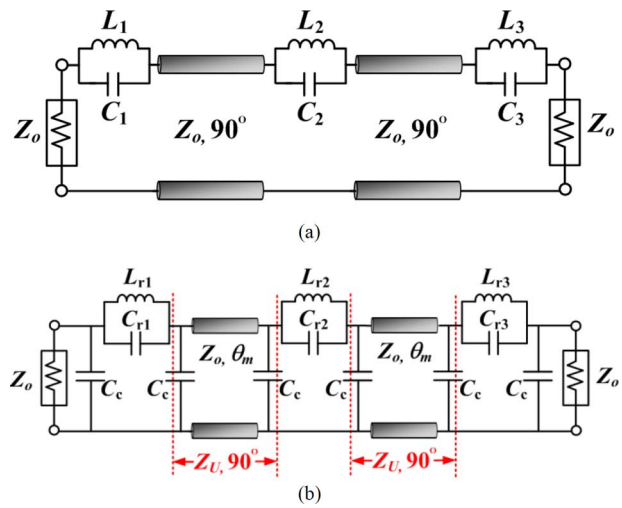

Fig. 7. Circuit models of the third-order bandstop filter: (a) prototype model and (b) modified model using multiple QRs.

IV. Synthesis of Multiorder QR-Based FFC

Considering the QR as a unit cell of the parallel LC resonator, this section will develop an FFC with cascading multiple QRs based on the classical microwave filter theory. Fig. 7(a) shows a prototype circuit model for the third-order bandstop filter. It consists of three parallel LC resonators and two 90° interconnection transmission lines with the characteristic impedance of Z_0. In accordance with the typical synthesis theory of the bandstop filter, the values of lumped elements can be determined by the lowpass prototype using bandstop frequency transformation.

Benefitting from the proposed QR structure, its simplified circuit model in Fig. 4(b) can be considered as a composite parallel LC resonator. By individually replacing the typical parallel resonators with the composite ones, Fig. 7(b) depicts the modified circuit model of the third-order bandstop filter; nevertheless, due to the existence of shunt-to-ground capacitors C_c, its effect

should be taken into consideration additionally. From Fig. 7(b), by shortening the electrical length to θ_m, the interconnection line shunted with capacitors C_c at both ends can be considered as an alternative 90° line with the characteristic impedance of Z_U. The corresponding *ABCD* matrices, therefore, should be equal to each other as in

$$[M_{C_c}] \times [M_{(Z_0,\theta_m)}] \times [M_{C_c}] = [M_{(Z_U,90^\circ)}] \tag{4}$$

where $[M_{Cc}]$ and $[M_{(\mathrm{Z}_0,\theta_m)}]$ are the *ABCD* matrices of one shunt capacitance of C_c and one transmission line of characteristic impedance Z_0 and electrical length θ_m, respectively. The detailed expansion of (4) is

$$\begin{bmatrix} \cos\theta_m - \omega_0 Z_0 C_c \sin\theta_m & jZ_0 \sin\theta_m \\ j\left(2\omega_0 C_c \cos\theta_m + \frac{1-Z_0^2(\omega_0 C_c)^2}{Z_0}\sin\theta_m\right) & \cos\theta_m - \omega_0 Z_0 C_c \sin\theta_m \end{bmatrix} = \begin{bmatrix} \cos(90^\circ) & jZ_U \sin(90^\circ) \\ \frac{j\sin(90^\circ)}{Z_U} & \cos(90^\circ) \end{bmatrix}. \tag{5}$$

By equalizing the left- and right-handed matrices of (5) the modified electrical length θ_m can be solved in terms of (ω_0, C_c, Z_0) as in

$$\theta_m = \cot^{-1}(\omega_0 Z_0 C_c). \tag{6}$$

Besides, the equivalent characteristic impedance Z_U is derived as

$$Z_U = Z_0 \sin\theta_m. \tag{7}$$

On the other hand, since the equivalent characteristic impedance of the interconnection line has been changed to Z_U, the lumped values of the middle parallel resonator L_{r2} and C_{r2} have to be re-normalized from Z_0 to Z_U. To maintain the same slope parameter, it can be calculated using the following expressions:

$$C_{r2} = C_2 \cdot (\frac{Z_0}{Z_U})^2, \tag{8}$$

$$L_{r2} = L_2 \cdot (\frac{Z_U}{Z_0})^2. \tag{9}$$

Fig. 8 shows the schematic of the implementation of the third-order QR-based FFC. Each unit cell is formed by the QR as a composite resonator. The electrical length θ_m is defined from the center to center of unit cells. An example of the synthesis procedures for third-order QR-based FFC is as follows.

1) Set the designed center frequency $f_{\mathrm{tz}} = 2.57$ GHz and FBW = 15% of the stopband. The geometrical parameters of each half-wavelength resonator on the PCB shown in Fig. 3(b) are co-designed to fit the resonant frequency at f_{tz}. In this example, $l_1 = 7.6$, $l_2 = 14.6$, $l_3 = 17$, $l_4 = 10$, $w = 0.2$, and $s_1 = 0.2$ (all units are in millimeters).
2) The Chebyshev's response of 0.1-dB ripple level is selected, and the corresponding low-pass prototype parameters are obtained from the tables [13] as $g_1 = 1$, $g_2 = 1.0316$, $g_3 = 1.1474$, $g_4 = 1.0316$, and $g_5 = 1$.
3) Using the bandstop frequency transformation, the typical lumped values of resonators (L_1, C_1), (L_2, C_2), and (L_3, C_3) in Fig. 7(a) can be calculated as Table I lists. It is worth noting that the 3-dB FBW of the prototype model is 10%, which is slightly narrower than the preliminary value of 15%, due to the impedance inverters formed by the transmission lines.
4) The lumped values of unit cells #1 and #3 in the modified model shown in Fig. 7(b) are intuitively obtained as $L_{r1} = L_{r3} = L_1 = 1.72$ nH and $C_{r1} = C_{r3} = C_1 = 2.21$ pF.
5) By utilizing (6), the modified electrical length θ_m (= 64.1 degree) is solved; meanwhile, the equivalent characteristic impedance Z_U can be attained from (7). Thus, the lumped values of the middle unit cell #2, L_{r2}(= 1.55 nH) and C_{r2}(=2.46 pF), can be obtained by using (8) and (9). For clarity, all of the synthesized LC values of both models for the third-order QR-based FFC are listed in Table I.
6) Using the design curves of L_r and C_r dependency on the spacing s_2 as shown in Fig. 6, the desired 1.72 nH of unit cells #1 and #3 (L_{r1} and L_{r3}) can be realized by $s_2 = 0.8$ mm, whereas the 1.92 nH of the unit cell #2 (L_{r2}) can be implemented by $s_2 = 0.6$ mm.

It is noted that the influence of capacitors C_c at the source and load terminations is minor for overall response and, thus, can be ignored for unit cells #1 and #3.

Based on the synthesis procedures from Steps 1)–6), all geometrical parameters of QR and the corresponding electrical parameters, such as LC values and θ_m, can be obtained. A third-order QR-based FFC can thus be realized by transferring θ_m to the physical length, which is 25.8 mm. Fig. 9(a) and (b) illustrates the simulated $|S_{11}|$ and $|S_{21}|$, respectively, by the full-wave simulation for this synthesized third-order QR-based FFC. The results predicted by the modified circuit model shown in Fig. 7(b) are also plotted in Fig. 9 for comparison. It is noted that all materials are assumed lossless in full-wave simulation because the losses are also not considered in the modified circuit model. It is clearly seen that the agreement between full-wave simulation and the modified circuit model is reasonably good

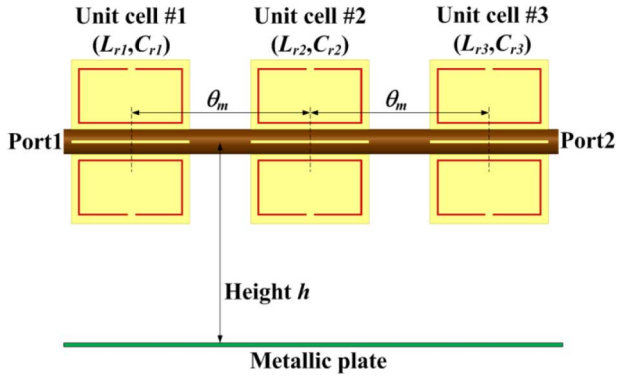

Fig. 8. Structure of the third-order QR-based FFC.

TABLE I
ELEMENT VALUES OF THE THIRD-ORDER BANDSTOP FILTERS

Prototype model	L_1=L_3	L_2	C_1=C_3	C_2	Z_0	E.L.
	1.72 nH	1.92 nH	2.21 pF	1.99 pF	180.2 Ω	90°
FFC model	L_{r1}=L_{r3}	L_{r2}	C_{r1}=C_{r3}	C_{r2}	Z_U	E.L.
	1.72 nH	1.55 nH	2.21 pF	2.46 pF	162.3 Ω	64.1°

Chebyshev response, 0.1-dB ripple level, and 15% FBW
f_0 = 2.57 GHz; C_c = 0.166 pF;
E.L.: electrical length of interconnection line

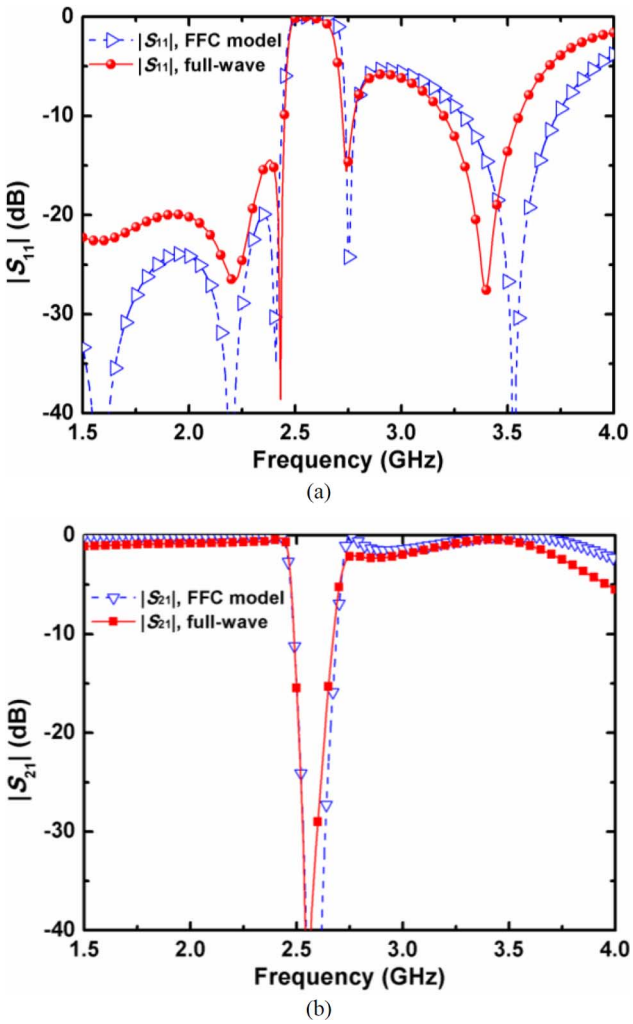

Fig. 9. S-parameters of the prototype model, FFC model, and full-wave simulation: (a) $|S_{11}|$ and (b) $|S_{21}|$.

for $|S_{11}|$ and $|S_{21}|$. As shown in Fig. 9(b), the full-wave simulated result for the frequency range of $|S_{21}| < -3$ dB is from 2.47 to 2.72 GHz, and the corresponding FBW is about 9.6%, which is almost identical to that of the prototype.

V. Measurements and Discussions

A. Suppression of the Cable Noise Currents

In order to evaluate the suppression of the cable noise currents, a third-order QR-based FFC designed in the previous section is fabricated. The schematic and photograph of the measurement environment are depicted in Fig. 10(a) and (b), respectively. First of all, a 50-Ω microstrip line fabricated on a 3 $\times$3 cm^2 FR-4 substrate is connected with a 20-cm-long coaxial cable. A 60 $\times$ 60 cm^2 aluminum plate is placed below the cable with height h. Meanwhile, a current probe encircles the coaxial cable to measure the noise currents on the cable shielding. The main purpose of connecting the PCB to the cable is to create an apparent ground discontinuity (or unbalance); dtherefore, significant noise currents can be induced on the cable shielding.

An Agilent network analyzer E5230A was used to measure S-parameters. The transmission coefficients $|S_{21}|$ between Port

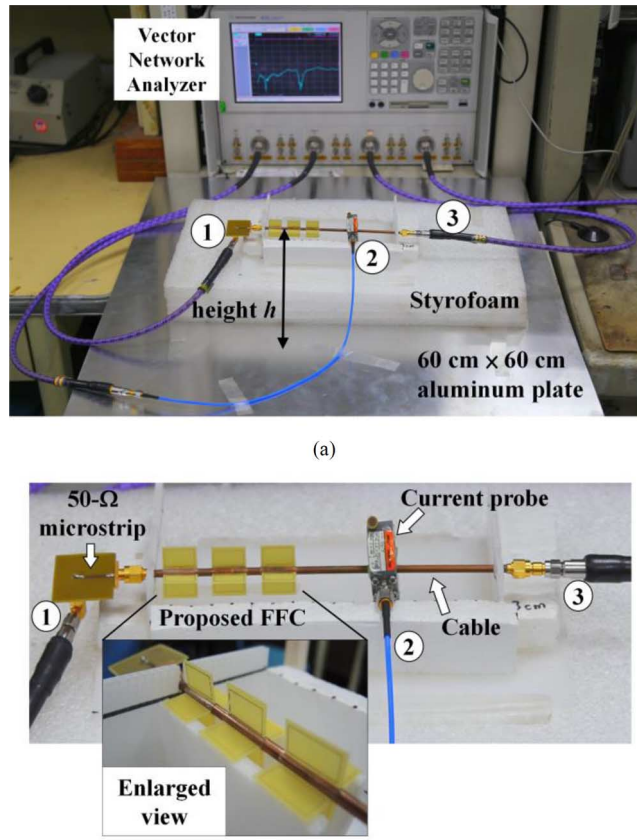

Fig. 10. Measurement environment for evaluating the performances of current suppression: (a) setup photograph and (b) enlarged view.

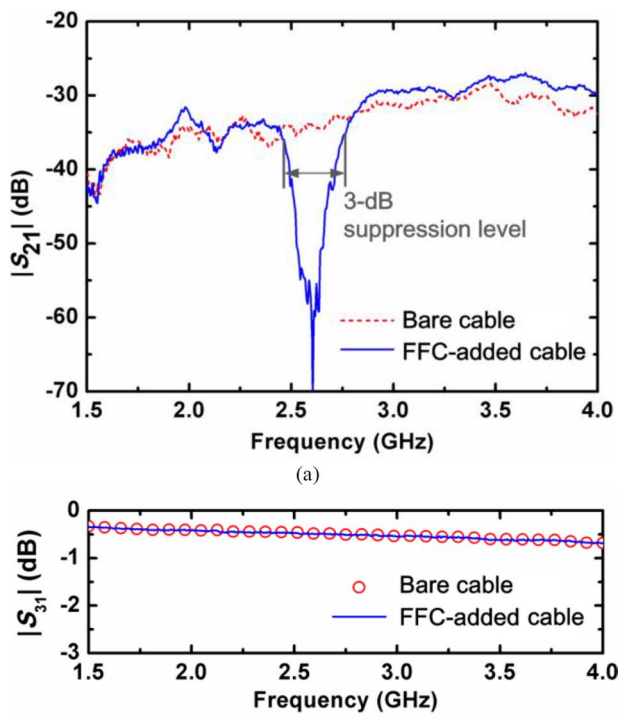

Fig. 11. Measured results using an F-2000 current probe: (a) $|S_{21}|$ and (b) $|S_{31}|$.

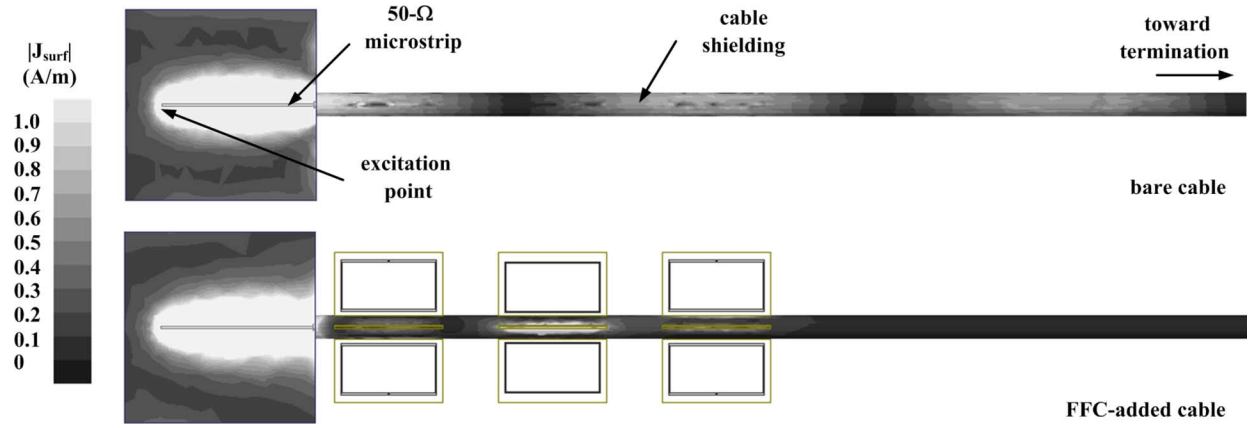

Fig. 12. Simulated current distributions on the PCB ground and the cable shielding using HFSS for the bare cable (upper) and the FFC-added cable (lower). (Solved frequency is at 2.6 GHz and the excited source is 1 W.).

TABLE II
CABLE CURRENT SUPPRESSIONS FOR DIFFERENT HEIGHTS

Height h	Highest suppression level	Frequency range of 3-dB suppression level
3 cm	36.1 dB	2.47 ~ 2.75 GHz
5 cm	33.8 dB	2.47 ~ 2.81 GHz
9 cm	25.6 dB	2.48 ~ 2.77 GHz
13 cm	31.3 dB	2.48 ~ 2.77 GHz
Plate removed	33.2 dB	2.48 ~ 2.76 GHz

1 (the excitation to the microstrip line) and Port 2 (the termination on the current probe) can evaluate the performances of noise current suppression. Port 3 is terminated. The current probe (model number: F-2000) with operation band from 100 MHz to 3 GHz is made by Fisher Custom Communications. In this measurement, the operating frequency is extended to 4 GHz. Since the transfer function of current probe is frequency-dependent, a calibration process is further required [14], [15]. After the current probe is calibrated, the measured $|S_{21}|$ will be proportional to the current noise on the cable shielding.

Initially, the height h is set as 3 cm, the measured $|S_{21}|$ and $|S_{31}|$ for the cases with and without using the third-order QR-based FFC along the cable are both shown in Fig. 11. It is seen $|S_{21}|$ for the case without adding the FFC is about -35 dB around 2.6 GHz. However, the noise currents are significantly reduced at the designed frequencies when the cable is surrounded by the proposed FFC. The highest suppression level is measured as 36 dB at 2.6 GHz. As shown in Fig. 11(a), the measured 3-dB suppression level is from 2.47 to 2.75 GHz (FBW $= 10.8\%$), which has a good agreement with the results by full-wave simulation and circuit model shown in Fig. 9(b). Meanwhile, as Fig. 11(b) plots, the measured $|S_{31}|$ between two cases are the same and it clearly indicates the proposed QR-based FFC doesn't influence the signal channel. In addition, the effect of height h on the FFC performance is also examined experimentally. It is varied from 3 to 13 cm, and finally the aluminum plate was removed. It is found the corresponding 3-dB suppression bandwidths for the FFC are nearly unchanged as shown in Table II. It can be explained when the height h is high enough, the influence of the large metal plate on the distribution of the magnetic fields induced from cable noise current becomes very small, which leads to the stable bandstop performances of the FFC.

Following the measurement setup environment shown in Fig. 10, the current distributions on the PCB ground and cable shielding are simulated by full-wave simulator and illustrated in Fig. 12. The excitation is located on the left-handed side of the 50-Ω microstrip line, and the right-handed side of the coaxial cable is terminated. The current distributions are simulated at the frequency of 2.6 GHz, where the excited source is set to 1 W. For the case without any FFC added, it is clearly seen that the noise currents are able to propagate along the cable shielding. Instead, for the case with FFC added, the noise currents are suppressed by the FFC and cannot pass through the cable.

B. Reduction of the Radiation Caused by Noise Currents

Fig. 13 shows the experimental setup for measuring radiation emissions from the noise currents on the cable shielding. The measurement was performed in a three-dimensional spherical near-field anechoic chamber along with the NSI-2000 software from Nearfield Systems Inc. In this setup, an Agilent network analyzer E5230A was used. The measuring antenna is an electrically-switch dual-polarized log-periodic antenna. The maximum sweep region of altitude angle is from $-165°$ to $165°$, so the rest of data will be calculated by interpolation. During the measurement, the termination on the cable is changed to short-ended loading; consequently, it will enhance the antenna gain, and thus a better signal-to-noise ratio can be achieved.

Fig. 14 plots the simulated and measured peak gains with and without adding the fabricated FFC from 2.3 to 2.9 GHz. Compared with the case without adding FFC (or bare cable), the frequency range of 3-dB reduction of peak gain is from 2.5 to 2.7 GHz, where the greatest reduction level is about 7 dB at 2.6 GHz. It is very close to our target center frequency of 2.57 GHz in the design stage. The deviation between simulation and measurement is mainly caused by the parasitic radiation from the excited cable in the anechoic chamber, which is too long to be included into the full-wave simulator. The radiation patterns at 2.6 GHz for both cases were also measured and shown

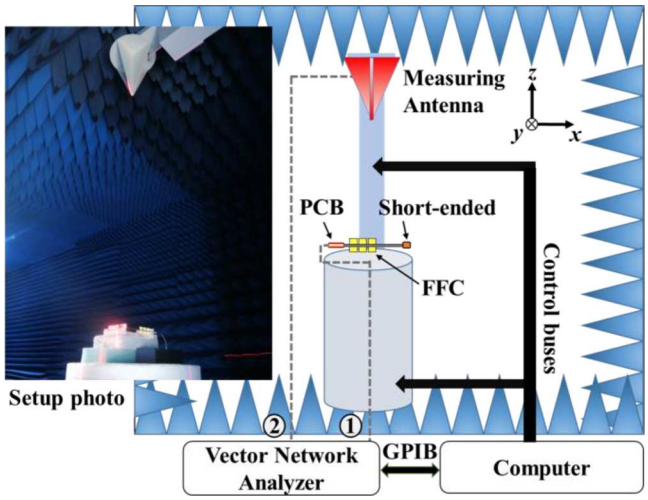

Fig. 13. Measurement setup of radiated emissions in an anechoic chamber.

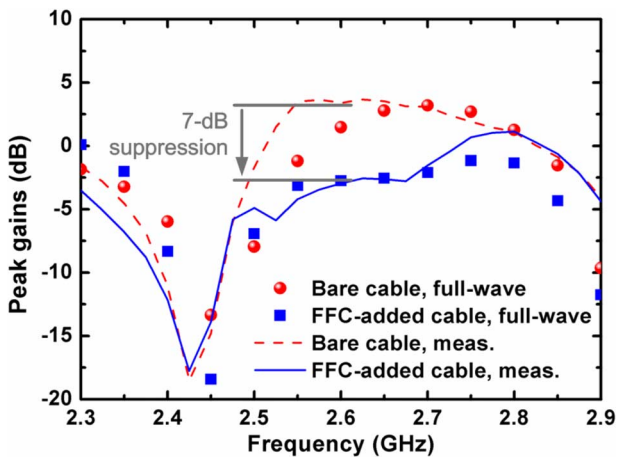

Fig. 14. Comparison of simulated and measured peak gains from 2.3 to 2.9 GHz.

in Fig. 15. The results measured on both *xy*-plane and *xz*-plane clearly indicate adding the third-order QR-based FFC along the cable has an effective performance on reducing radiated powers caused by the noise currents. The maximum power reduction can reach about 15 dB for both planes. On the other hand, it is worth noting the level of radiation reduction is not such high as the level of noise current suppression. Also, the FFC-added cable radiates more than the bare cable at some angles as shown in Fig. 15. They can be explained when the strongly reflected noise currents flow back to the ground discontinuity between the cable and PCB, part of reflected energy will be radiated and thus it degrades the performances. Practically, these ground interconnections such as USB connectors and other high-speed interfaces are surrounded by grounded metallic boxes; consequently, such a "re-radiation" problem induced by reflected currents could be well shielded.

VI. Conclusion

In this paper, based on the QRs, a multiorder FFC to suppress the noise currents on cable shielding is proposed. The equivalent circuit model of a unit-cell QR considering the magnetic

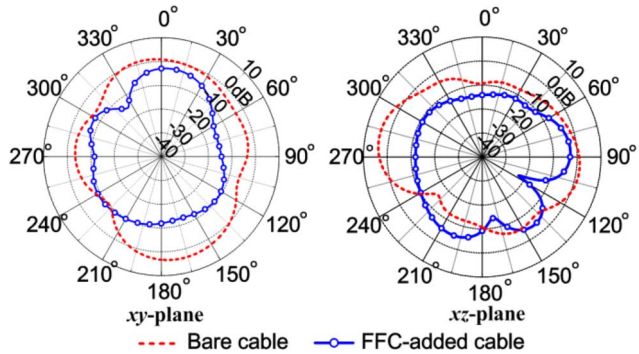

Fig. 15. Measured radiation patterns of the xy-plane and xz-plane at 2.6 GHz.

coupling between resonators and cable shielding has been developed and used to explain the noise current suppression mechanism. By cascading multiple QRs and employing microwave filter theory, a multiorder QR-based FFC is also proposed with an effective noise current suppression at a specific frequency range. The circuit model for the multiorder FFC is developed, and the corresponding synthesis procedure for the FFC is also established. A third-order QR-based FFC is fabricated by following the synthesis procedures, and performances in the reduction of noise current and radiation are both measured. It is found that this FFC achieves high-level suppression (about 36 dB) of noise currents at gigahertz frequency ranges. The radiation peak gain can also be reduced by 7 dB at the center frequency. The measured results also show good agreement with the circuit-modeled and full-wave simulations.

By taking advantage of the magnetic-coupling mechanism, the key difference is that the metallic strips of QR-based FFC do not need to directly attach to the shielding of cable. The QR-based FFC can attach on a cable without damaging the cable jacket. For practical usage, with the assistance of a plastic holder, the QR-based FFC can be readily installed on cables, such as with a traditional ferrite choke. By cascading them, the multiorder FFC can be utilized on bended cables as demonstrated in the inset of Fig. 1. Nonetheless, compared with commercial ferrite chokes, the size of QR-based FFC is larger and the operating bandwidth is much narrower. To make the QR-based FFC much easier to utilize practically, further circuit miniaturization and wideband design will be the interesting and critical topics we will focus on.

Appendix

From Fig. 4(a), since the resonators are designed in the same patterns, it can be considered as a single resonator with the equivalent coupling coefficient k_t as Fig. 16(a) depicts. And, therefore, k_t can be calculated as in

$$k_t = \sqrt{k_1^2 + k_2^2 + k_3^2 + k_4^2} \tag{A1}$$

where k_j is the coupling coefficient between the cable and jth resonator. Next, by introducing the T-type model of the K-inverter [13], the decoupled form can be represented as Fig. 16(b) shows and the L_m is expressed as

$$L_m = k_t \sqrt{L_c L_h}. \tag{A2}$$

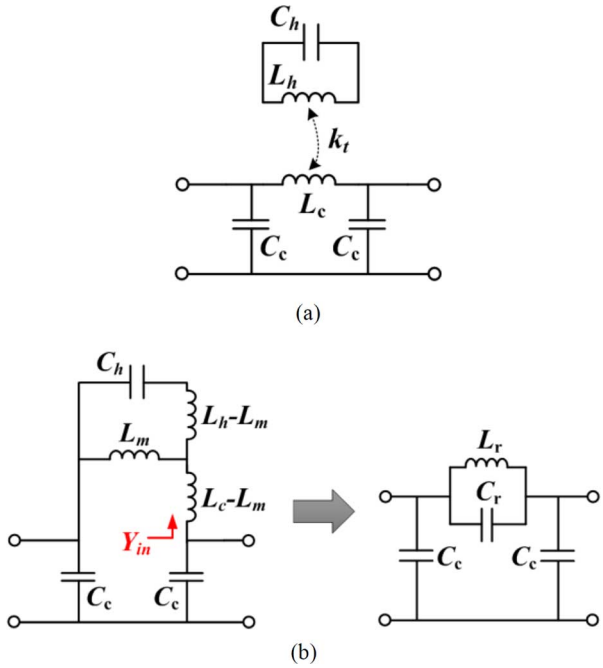

Fig. 16. (a) Equivalent single-resonator model and (b) the corresponding decoupled model.

In accordance with the decoupled-form model, the admittance Y_{in} can be derived as

$$Y_{\text{in}} = \frac{j(\omega^2 L_h C_h - 1)}{\omega L_c[\omega^2 L_h C_h(k_t^2 - 1) + 1]}. \tag{A3}$$

The bandstop response occurs when Y_{in} is equal to zero and, thus, the corresponding resonant frequency is

$$\omega_0 = \frac{1}{\sqrt{L_h C_h}}. \tag{A4}$$

In addition, by differentiating (A3), the derivative formula can be rearranged as in (A5); furthermore, the slope parameter of susceptance at the resonant frequency can be further calculated as

$$\frac{\partial Y_{in}(\omega)}{\partial \omega} = \frac{jL_c[(\omega^2 L_h C_h + 1) - (k_t^2 - 1)(\omega^4 L_h^2 C_h^2 - 3\omega^2 L_h C_h)]}{\{\omega L_c[\omega^2 L_h C_h(k_t^2 - 1) + 1]\}^2} \tag{A5}$$

$$b_{in} = \frac{\omega_0}{2}\frac{\partial Y_{in}(\omega)}{\partial \omega}\bigg|_{\omega=\omega_0} = \frac{1}{\omega_0(k_t^2 L_c)}. \tag{A6}$$

From (A5), for a narrow frequency band, it clearly indicates that the behavior of Y_{in} can be equivalent to a parallel LC tank formed by L_r and C_r, which are expressed as

$$L_r = k_t^2 L_c \tag{A7}$$

$$C_r = \frac{1}{\omega_0^2 k_t^2 L_c}. \tag{A8}$$

When the equivalent coupling coefficient k_t goes larger, it points out the susceptance slope parameter b_{in} will become smaller and will reasonably lead to a wider stopband bandwidth.

It is worth noting that the derivations are hereby to demonstrate that the QR-based FFC can be considered as a parallel LC tank (in a narrow band) shown in Fig. 4(b). From the perspective of circuit design, there is no need to know the exact value of k_t; therefore, it would be much more straightforward to extract the values of L_r and C_r as described in Section III.

REFERENCES

[1] T.-L. Wu, F. Buesink, and F. Canavero, "Overview of signal integrity and EMC design technologies on PCB: fundamentals and latest progress," *IEEE Trans. Electromagn. Compat.*, vol. 55, no. 4, pp. 624–638, Aug. 2013.

[2] H.-W. Shim and T. H. Hubing, "Model for estimating radiated emissions from a printed circuit board with attached cables due to voltage-driven sources," *IEEE Trans. Electromagn. Compat.*, vol. 47, no. 4, pp. 899–907, Nov. 2005.

[3] H. Ke, K. Morishita, T. H. Hubing, N. Kobayashi, and T. Harada, "Modeling radiated emissions due to power bus noise from circuit boards with attached cables," *IEEE Trans. Electromagn. Compat.*, vol. 51, no. 2, pp. 412–416, May 2009.

[4] C. Su and T. H. Hubing, "Improvements to a method for estimating the maximum radiated emissions from PCBs with cables," *IEEE Trans. Electromagn. Compat.*, vol. 53, no. 4, pp. 1087–1091, Nov. 2010.

[5] T. Fukasawa, T. Yanagi, H. Miyashita, and Y. Konishi, "Extended S-parameter method including radiation pattern measurements of an antenna," *IEEE Trans. Antennas Propag.*, vol. 60, no. 12, pp. 5645–5653, Dec. 2012.

[6] H. H. Park, H.-B. Park, and H. S. Lee, "A simple method of estimating the radiated emission from a cable attached to a mobile device," *IEEE Trans. Electromagn. Compat.*, vol. 55, no. 2, pp. 257–264, Apr. 2013.

[7] J. Urabe, K. Fujii, Y. Dowaki, Y. Jito, Y. Matsumoto, and A. Sugiura, "A method for measuring the characteristics of an EMI suppression ferrite core," *IEEE Trans. Electromagn. Compat.*, vol. 48, no. 4, pp. 774–780, Nov. 2006.

[8] N. V. Blaz, M. D. Lukovic, M. V. Nikolic, O. S. Aleksic, L. D. Zivanov, and L. S. Lukic, "Analysis of a Mn-Zn ferrite bundle EMI suppressor using different suppressing principles and configurations," *IEEE Trans. Magn.*, vol. 49, no. 8, pp. 4851–4857, Nov. 2013.

[9] L. Loizou, J. Buckley, B. O'Flynn, J. Barton, C. O'Mathuna, and E. Popovici, "Design and measurement of a planar dual-band antenna for the tyndall multiradio wireless sensing platform," in *Proc. IEEE Sensor Appl. Symp.*, Feb. 2013, pp. 11–14.

[10] C. Icheln, J. Krogerus, and P. Vainikainen, "Use of balun chokes in small-antenna radiation measurement," *IEEE Trans. Instrum. Meas.*, vol. 53, no. 2, pp. 498–506, Apr. 2004.

[11] S.-C. Jung, T.-W. Jung, and J.-M. Woo, "Design of sleeve dipole antenna for suppressing leakage current on a coaxial cable," *IEEE Antennas Wireless Propag. Lett.*, vol. 13, pp. 459–462, 2014.

[12] C. R. Paul, "A comparison of the contributions of common-mode and differential-mode currents in radiated emissions," *IEEE Trans. Electromagn. Compat.*, vol. 31, no. 2, pp. 189–193, May 1989.

[13] J. S. Hong and M. J. Lancaster, *Microstrip Filters for RF/Microwave Application*, 2nd ed. Hoboken, NJ, USA: Wiley, 2001.

[14] Y. Kayano, M. Tanaka, J. L. Drewniak, and H. Inoue, "Common-mode current due to a trace near a PCB edge and its suppression by a guard band," *IEEE Trans. Electromagn. Compat.*, vol. 46, no. 1, pp. 46–53, Feb. 2004.

[15] C.-Y. Ho, K.-S. Chen, and T.-S. Horng, "Estimating the reduction of radiated emissions from microstrip components using network analyzer with a bulk current injection probe," *IEEE Microw. Wireless Compon. Lett.*, vol. 23, no. 2, pp. 108–110, Feb. 2013.

Ying-Cheng Tseng was born in Tainan, Taiwan, in 1987. He received the B.S. and M.S. degrees in electrical engineering from National Taiwan University of Science and Technology, Taipei, Taiwan, in 2010 and 2012, respectively, where he is currently pursuing the Ph.D. degree in communication engineering from the National Taiwan University, Taipei, Taiwan.

His research interests include high-frequency electromagnet interference elimination, passive microwave components, and integration of RF/millimeter-wave front-end systems.

Hui-Ling Ting received the M.S. degree in communication engineering from National Taiwan University, Taipei, Taiwan, in 2006 and 2008, where she is currently pursuing the Ph.D. degree in communication engineering.

She is also a Technical Specialist with the Bureau of Standards, Metrology and Inspection, MOEA, Taipei. Her current research interests include electromagnetic compatibility and microwave circuits design.

Tzong-Lin Wu (S'93–M'98–SM'04–F'13) received the B.S.E.E. and Ph.D. degrees in electrical engineering from National Taiwan University (NTU), Taipei, Taiwan, in 1991 and 1995, respectively.

From 1995 to 1996, he was a Senior Engineer at Micro-electronics Technology Inc., Hsinchu, Taiwan. In 1996, after receiving the Ph.D. degree, he joined the Central Research Institute of the Tatung Company, Taipei, where he was involved in the analysis and measurement of electromagnetic-compatibility/electromagnetic-interference (EMC/EMI) problems of high-speed digital systems. In 1998, he decided to pursue an academic career and accepted a position in the Electrical Engineering Department at National Sun Yat-Sen University, Kaohsiung, Taiwan. Since 2006, he has been a Professor in the Department of Electrical Engineering and Graduate Institute of Communication Engineering (GICE), NTU. He was appointed Director of the GICE and Communication Research Center at NTU in 2012. GICE is among the best institutes in Taiwan with 41 faculty members and about 450 graduate students. The research direction of GICE includes electromagnetic wave, communication, and multimedia. Currently, he is Associate Editor of IEEE TRANSACTIONS ON ELECTROMAGNETIC COMPATIBILITY and IEEE TRANSACTIONS ON COMPONENTS, PACKAGING, AND MANUFACTURING TECHNOLOGIES. His research interests include EMC/EMI and signal/power integrity design for high-speed digital/optical systems.

Prof. Wu received the Excellent Research Award and the Excellent Advisor Award from National Sun Yat-Sen University in 2000 and 2003, respectively; the Outstanding Young Engineers Award from the Chinese Institute of Electrical Engineers in 2002; and the Wu Ta-You Memorial Award from the National Science Council (NSC) in 2005; Outstanding Research Award from NSC in 2010 and 2014; and the IEEE TRANSACTIONS ON ADVANCED PACKAGING Best Paper Award in 2011. He has served as the Chair of the Institute of Electronics, Information and Communication Engineers (IEICE) Taipei Section in 2007–2011; the Treasurer of the IEEE Taipei Section in 2007–2008; and was a member of the Board of Directors of the IEEE Taipei Section in 2009–2010 and 2013–2016. He served the IEEE EMC Society as a Distinguished Lecturer from 2008 to 2009. He was Co-Chair of the 2007 IEEE Electrical Design of Advanced Packaging and Systems (EDAPS) Workshop, General Chair of the 2015 Asia Pacific EMC Symposium (APEMC), and Technical Program Chair of the 2010 and 2012 IEEE EDAPS Symposiums.